Available online at www.sciencedirect.com

jmr&t
Journal of Materials Research and Technology

journal homepage: www.elsevier.com/locate/jmrt

Original Article

Influence of cold deformation on microstructure, crystallographic orientation and tensile properties of an experimental austenitic Fe–26Mn-0.4C steel

Marcos Natan da Silva Lima [a,c], *Rodrigo de Carvalho Paes Loureiro* [a], *Miloslav Béreš* [a], *Mohammad Masoumi* [b], *Jessica Calvo Muñoz* [c], *Samuel Filgueiras Rodrigues* [d,*], *Hamilton Ferreira Gomes de Abreu* [a], *José María Cabrera Marrero* [c]

[a] *Materials Characterization Laboratory (LACAM), Department of Metallurgical and Materials Engineering, Federal University of Ceará, Campus Do Pici, Bloco 729, Fortaleza 60020-181, Ceará, Brazil*
[b] *Center for Engineering, Modeling and Applied Social Sciences, Federal University of ABC, Santo André, São Paulo, 09210-580, Brazil*
[c] *Processes for Conformation of Metallic Materials (PROCOMAME), Department Materials Science and Metallurgical Engineering, Universitat Politècnica de Catalunya: Barcelona, Catalunya, Bl. I, 08930, Spain*
[d] *Graduate Program in Materials Engineering, Federal Institute of Education, Science and Technology of Maranhao, Sao Luis, Maranhao, 65030-005, Brazil*

ARTICLE INFO

Article history:
Received 24 March 2022
Accepted 2 May 2022
Available online 11 May 2022

Keywords:
Austenitic high manganese steel
Mechanical twinning
Lattice distortion
Grain boundaries
Texture

ABSTRACT

The correlation between microstructure, crystallographic orientation and grain boundaries characteristics of an austenitic high manganese steel was systematically investigated. The as-received and cold-rolled specimens with 50% and 70% reduction were analyzed using Scanning Electron Microscopy (SEM), Electron Back-Scattered Diffraction (EBSD) and X-ray diffraction techniques. A significant increase in the fraction of low-energy Σ3 twin boundaries, from 16.21% to 24.41%, was found in the 70% deformed sample. This was coupled with the formation of {011} austenitic structure, and occurrence of twinning-induced plasticity. The ductile-brittle fracture mode observed in the 70% cold rolled sample, which can be attributed to the formation of the high fraction of low-energy Σ3 twin boundaries, minimized both the localized stored strain energy and lattice misfit and promoted dislocation glide. A potential employment of the investigated steel in the petroleum industry is discussed.

* Corresponding author.
E-mail address: samuel.filgueiras@ifma.edu.br (S.F. Rodrigues).
https://doi.org/10.1016/j.jmrt.2022.05.020

1. Introduction

Recently, austenitic (high-Mn) steel has been receiving particular attention due to excellent combination of high ductility, high strength, low thermal expansion coefficient, good fatigue property, toughness and formability associated with the twinning-induced plasticity (TWIP) effect. In face centered cubic (FCC) austenitic high-Mn steel with low stacking fault energy (SFE), i.e. less than 40 mJ/m^2, mechanical twins are formed during plastic deformation at room temperature. The twins act as obstacles to dislocation glide, reducing the effective mean free path for dislocation gliding in {111} slip planes [1]. The deformation mechanisms of these steels, especially dislocation slip, mechanical twinning and strain-induced transformation, are influenced by the stacking fault energy (SFE), which is controlled by chemical composition and temperature. Increasing the dislocation density coupled with altering the dislocation structures by mechanical twinning, also known as the dynamic Hall-Petch effect, leads to an increase in work-hardening rate and strength at the cost of elongation [2,3].

A cold working process is suggested to increase both the yield and ultimate tensile strength of high-Mn austenitic steels. Although cold working increases the tensile strength, it also increases the notch sensitivity and promotes early crack initiation and propagation at grain boundaries and/or at inclusions [4]. Although the influence of cold-deformation on microstructure and mechanical properties has been well investigated, a limited research has been conducted on the role of crystallographic orientation changes during cold-rolling. Therefore, it is extremely important to understand the distribution of local strain along particular crystallographic planes and directions in the FCC structure. Such knowledge can provide information about the nature of anisotropy in strain attributed to crystal orientation and action can be taken in order to avoid the formation of crack initiation site and crack propagation when the material is under services [4].

Additionally, another differential point of this work is related to the chemical composition of the TWIP steel evaluated. It is a steel without aluminum, with a high chromium content, to increase corrosion protection and the presence of copper, since this element improves the resistance of steels to atmospheric corrosion three to five times compared to unalloyed steels [5]. Moreover, an increase in total elongation resulting from a more gradual decrease in the rate of strain hardening was reported for the TWIP steel with Cu added [5]. It was also reported that TWIP steels with Cu additions presented higher resistance to delayed fracture compared to TWIP without Cu steels. All these properties favor the application of TWIP steels containing Cu in the petroleum industry [5]. To the best of our knowledge, little attention has been devoted to investigating the role of crystallography of the high-Mn austenitic steel studied in this work. This investigation thus aimed to assess the detailed parameters which govern the microstructure features of the metal as received and under cold rolling process.

2. Experimental procedure

An experimental austenitic high-Mn steel was studied in the paper as a possible substitute to the materials conventionally employed in petroleum industry, such as pearlitic steels and high-strength low-alloy steels. The material was delivered as thick sheets with the chemical composition, determined by Optical Emission Spectroscopy (OES) in a Shimadzu Spectrometer, model PDA 7000, of 0.45C–26.05Mn-3.4Cr-0.45Cu, balance Fe (wt.%). The SFE was evaluated to be ~21 mJ/m2 at room temperature according to the thermodynamic model [6,7]. The material was manufactured by blast furnace steelmaking process, and hot rolled to final thickness of 20 mm. Samples with dimensions 20 × 12 × 12 mm^3 were extracted from the sheets and studied in the as-received condition and after cold rolling. The cold rolling was conducted at room temperature using a laboratory rolling mill (Coelho Machines Manufacturer/Model LE-200B) at a rotational speed of 8 m/min. Seven passes were required to obtain a 50% total reduction, whereas with ten passes a 70% total reduction was achieved. Then, the samples were prepared using standard metallographic procedures, including grinding (#120 to #1200 SiC papers) followed by mechanical polishing using 6, 3, and 1 μm diamond paste and finally 0.4 mm colloidal silica suspension. A chemical etching with (40% HNO_3 + 60% H_2O) solution was used for a time of 3 s.

Microstructural studies were carried out along the rolling direction (RD)–normal direction (ND) plane in the received and deformed specimens using Optical Microscopy (OM) and Field Emission Gun Scanning Electron Microscopy (FEGSEM) FEI Quanta FEG 450.

X-ray diffraction (XRD) method was used to characterize the phase structure in the investigated samples. XRD was performed using a Panalytical X'Pert Pro diffractometer equipped with Co ($K\alpha_1$ = 1.78897 Å) radiation source. The plane distance of interfered atomic planes was calculated by Bragg's Law ($2 \cdot d \cdot sin\theta = n \cdot \lambda$) where d is the spacing between atomic planes, 2 θ is the diffraction angle, n is an integer and λ is the wavelength. The position of the diffraction peak can be affected by homogeneous and inhomogeneous local strains, which can be calculated by the Sherrer formula (Eq. (1)) [8]:

$$D = \frac{C \cdot \lambda}{\beta \cdot \cos\theta} \quad (1)$$

where, D is the crystallite size, C is a constant related to crystallite and normally equals to 0.91, λ is the incidence wavelength, β is the full width at half maximum (FWHM) of diffraction peak and θ is the half of diffraction angle.

Macrotexture measurements were conducted using a Panalytical X'Pert Pro diffractometer equipped with a texture goniometer, using Co radiation. The measurements were performed in the reflection mode on a 5° grid at a sample tilt of up to 85°. Orientation Distribution Functions (ODFs) of each sample were calculated from the measured pole figures using the MTEX open-source software toolbox [9]. The $\varphi_2 = 0°$ and 45° section of Euler space was used to display the computed ODFs.

Samples for Electron Backscatter (EBSD) measurements were prepared by grinding using #120 to #1200 SiC papers. This

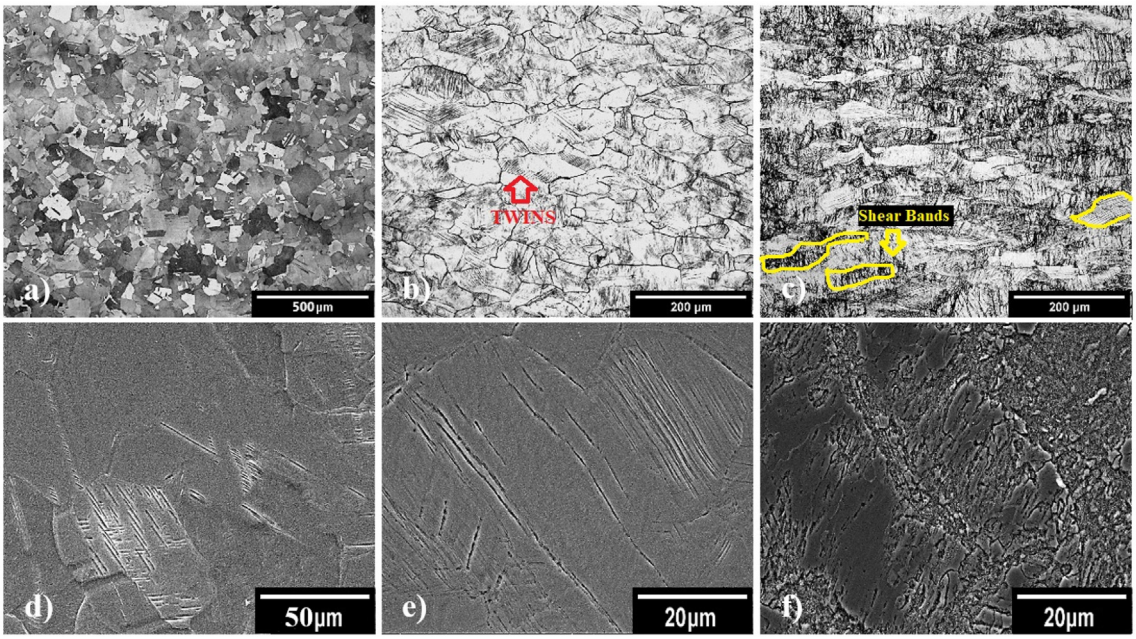

Fig. 1 – Optical micrographs of samples (a) as-received, cold-rolled to (b) 50% and (c) 70% reduction. FEGSEM secondary electron micrographs of specimens (d) as-received, cold-rolled to (e) 50% and (f) 70% reduction. (Mechanical twins are depicted with red and shear bands are depicted with yellow).

was followed by electrolytic polishing solution (60% ethanol + 34% n-butanol + 6% perchloric acid), with a voltage of 20 V and current ranging from 0 to 2 A for 1–3 min. Finally, the specimens were polished with 0.05 μm colloidal silica slurry for 15 min.

FEI Quanta FEG 450 and FEI Quanta FEG 650 FEGSEM microscopes operated at 20 kV were used to collect the EBSD data. The working distance was set to about 17 mm with a tilt angle of 70°. Microtexture analyses were conducted using the Channel 5 and ATEX data processing software package. ODFs were determined from EBSD maps through the statistical Kernel density estimation method and plotted at constant Euler angles of $\varphi_2 = 45°$.

Tensile tests were performed at room temperature on samples with a gauge length of 16 mm and overall length of 55 mm using MTS 370 universal testing machine. ASTM E8 standard recommendation for subsize specimens was followed, establishing that the length of the grip section was large enough to allow the specimen to extend into the grips in a distance equal to two thirds or more from the length of the grips. The strain rate applied was 2×10^{-2} s^{-1}. Six specimens were tested for each condition including as-received and cold-rolled samples submitted to 50% and 70% reduction. The fractured surfaces of tensile samples were subjected to fractographic analysis using FEGSEM.

3. Results and discussion

3.1. Microscopy analysis

The OM and SEM micrographs at cross-section of the as-received specimen, 50% and 70% reduced under cold-rolled samples are shown in Fig. 1. The as-received sample, Fig. 1a, exhibited a fully recrystallized refined austenitic microstructure, with mostly equiaxed grains containing abundant thermal twins originated from the hot-rolling process, and few mechanical twins originated from the sample preparation. This is consistent with observation reported by Florez et al. [10]. The determined micro-hardness value was 202 ± 5 HV. Mechanical twins (red arrow) gradually increased in the 50% cold-rolled sample, Fig. 1b. The formation of mechanical twins is associated with low Stacking Fault Energy (SFE) of this alloy system. The micro-hardness values also increased to 420 ± 8 HV by applying a 50% rolling reduction. In samples subjected to a 70% cold rolling reduction, the mechanical induced-twinning occurred on deformation shear bands, resulting in an increase of the micro-hardness to about 502 ± 7 HV. Austenitic grains showed a heterogeneous morphology structure due to the formation of shear bands resulting from the rolling process. The shear bands intersection formed a spatial network, which is shown in Fig. 1c (depicted with yellow). The gradual development of shear bands occurs with the progressing degree of the cold rolling reduction, and comprised ultrafine grains coupled with dislocation tangles structure as reported by Kowalska and Kowalski [11].

3.2. XRD investigation

Fig. 2 presents the XRD patterns of all investigated specimens. The single austenite phase was observed in the as-received sample. The XRD patterns of cold rolled specimens confirmed the absence of any other phases (including α' and/or ε martensite). Therefore, deformation-induced martensitic transformation did not occur even in samples subjected to a 70% cold rolling reduction. The high Mn-content (26.05 wt.%)

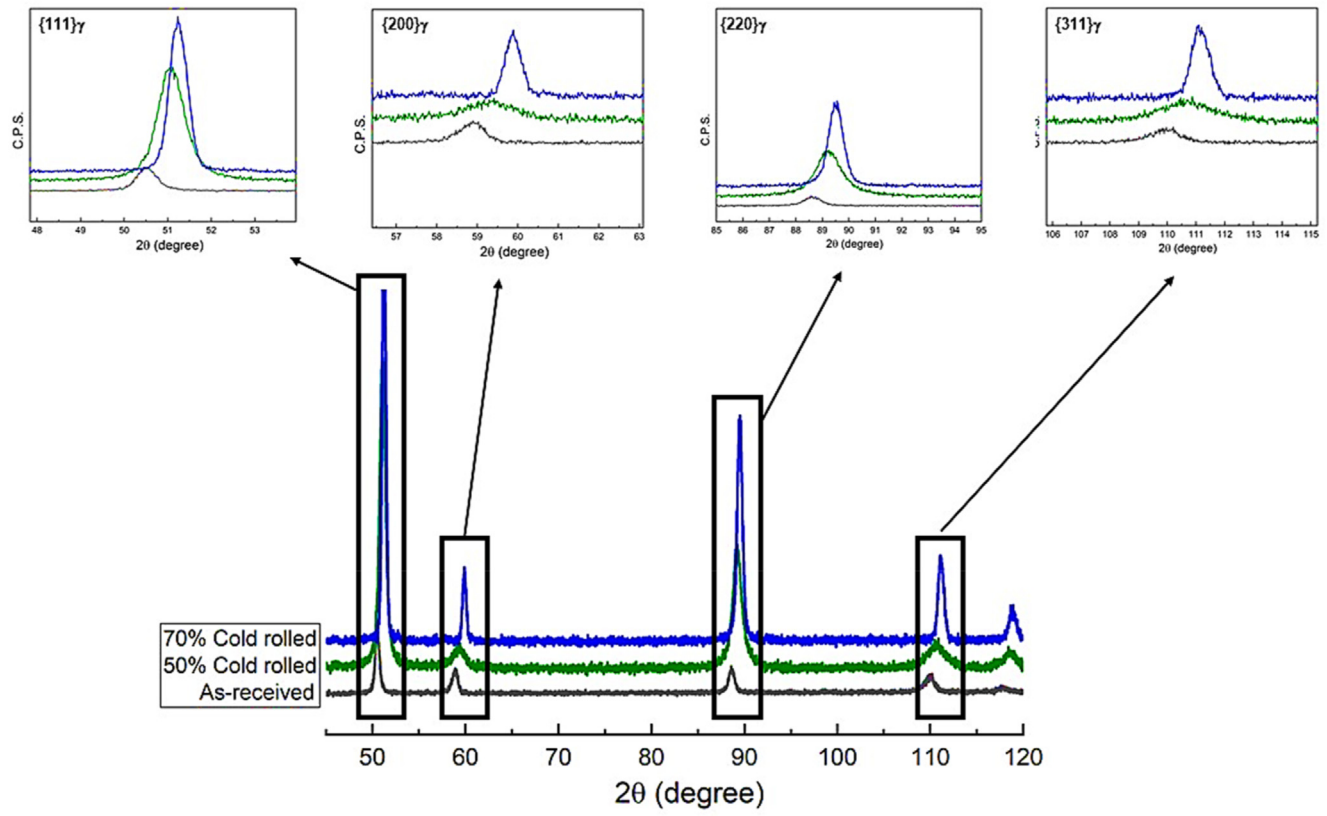

Fig. 2 – XRD patterns of all samples.

as austenite stabilizer suppress the deformation-induced martensitic phase transformation. Diffraction peaks shifted towards higher diffraction angles and peak broadening was observed in the cold deformed specimens. According to Berkum et al. [12] single-dimensional defects such as dislocations can cause peak broadening, and planar defects, and twins can cause displacement of the peak position diffraction angles. This can be attributed to an increase in dislocation density in addition to a lattice distortion induced by plastic deformation [13]. The asymmetric diffraction peak is another consequence of the lattice distortion, and is an indication of formation of Coincidence Site Lattice (CSL) boundaries, including twinning [14].

The high dislocation density due to cold rolling causes a localized lattice distortion that altered the peak shape of diffracted peak patterns. Notably, peak broadening value can represent an indirect evidence of dislocation density in metallic materials. Thereby, the dislocation densities of investigated as-received and cold-rolled specimens to 50% and 70% reduction were estimated by the method proposed by Ungar [14] and the modified Williamson-Hall method and where were determined to be $2.23 \times 10^{13}\ m^{-2}$, $5.13 \times 10^{14}\ m^{-2}$, and $1.51 \times 10^{15}\ m^{-2}$, respectively. The increase in dislocation density generated during cold rolling causes greater distortion of the crystal lattice, increasing the energy stored in the material. As a consequence, there is an elongation of the grains, formation of shear bands and twin contours, which agrees with hardness results reported before.

3.3. *Inverse Pole Figure (IPF) map and ODFs studies*

Inverse Pole Figure (IPF) map and ODFs at $\varphi_2 = 0°$ and 45° sections in the Euler $(\varphi_1, \varphi, \varphi_2)$ space of investigated samples are presented in Fig. 3. For rolled strips, the crystallographic orientations are represented by the Miller index (hkl)[uvw] combining of crystallographic plane and direction. In this case, (hkl) is the plane parallel to the rolling plane (RP), and [uww] is the direction parallel to the rolling direction (RD). The results revealed that mainly {001}//RP crystallographic orientations were predominant in the as-received sample. This was attributed to the recrystallized grains which were formed during the hot rolling process. At the same time, sharp orientation change to {110}//RP textures were found in samples subjected to cold-rolling. A remarkable texture reorientation took place during cold-rolling to 50% reduction, where Goss (110)[001], Brass (110)[2 $\bar{2}$ 1], and {110}<112> texture components were dominant by increasing the cold rolling reduction [15].

Although the development of Brass to Goss texture components due to the lattice shear invariant [15], the development of sharp {110}<112> crystallographic texture is commonly observed in FCC metals with low SFE, i.e.<25 mJm^{-2} [16]. In austenitic high-Mn steel, slip and twinning is the predominant plastic deformation mechanism and the deformation mode is governed by the value of the SFE. The slip takes place on the most dense-packed planes and directions

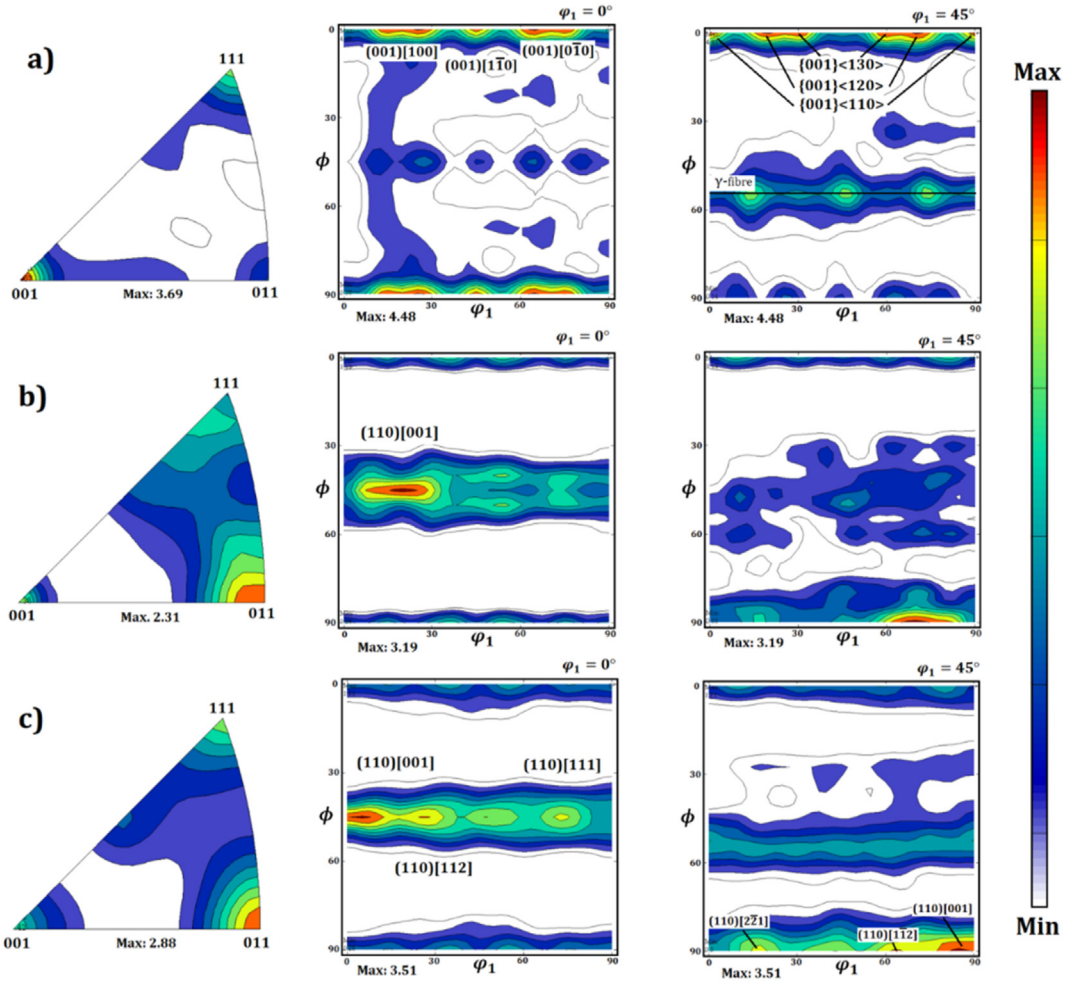

Fig. 3 – Inverse Pole Figure map and Orientation Distribution Function at $\varphi_2 = 0^\circ$ and 45° sections of samples (a) as-received, cold-rolled to (b) 50% and (c) 70% reduction.

as a function of the crystal structure. For instance, the {111}<110> is the main slip system in the FCC materials. With decreasing the SFE values, the ability of plastic deformation by slip decreases, thereby, deformation occurs mainly by twinning mechanism. In this scenario, the twinning mainly takes places on {111} twinning planes and <112> twinning direction [17]. Moreover, the development of τ-fiber corresponds to orientations having a <110> direction along the line, in the section, i.e., {110}<001> orientation, as reported by Hirsch et al. [18]. The drastic reduction of cleavage (001) planes accompanied by a high fraction of denser atomic (110) planes may facilitate slip under external load application.

Shear deformation induced by the friction between of rolled sample and the rolls is the main reason of crystallographic texture formation especially at the surface. In order to demonstrate the influence of shear stress caused by rolling deformation, skeleton plots for main texture fiber including (001), (111), and (101) crystallographic planes oriented along rolling plane were plotted from their ODFs and are presented in Fig. 4. The as-received hot-rolled austenitic steels had predominant (001) and (111) crystallographic texture parallel to the rolling plane due to the dynamic recrystallization during hot deformation [16]. Meanwhile, the intensity (i.e., normalized number of grains) of these fibers reduced by increasing the cold rolled reduction. On the other hand, the (101) grains oriented along rolling plane were developed gradually with increasing the cold deformation. The formation of shear bands in austenitic grains cased a rotation of in-band crystal into the <110> crystal axis to increase the fraction of softened austenite phase by reducing the stored-energy by means of the mechanism known as strain induced boundary migration [19,20]. Recently, Kamali et al. [21] reported that the (110) oriented austenitic grains encompass a higher fraction of deformation due to the slip activity.

The orientation image maps (OIMs) of as-received and cold-rolled samples to 50% and 70% reduction obtained by EBSD technique are depicted in Fig. 5. These figures revealed that by increasing the amount of deformation, a gradual orientation gradient develops within the grains. The as-received sample had (001)[100] and (001)[120] preferred crystallographic orientations. The presence of cleavage cube (001)[100] component could be related to the fine columnar grains developed during solidification in the direction of the maximum heat conduction accompanied with dynamic

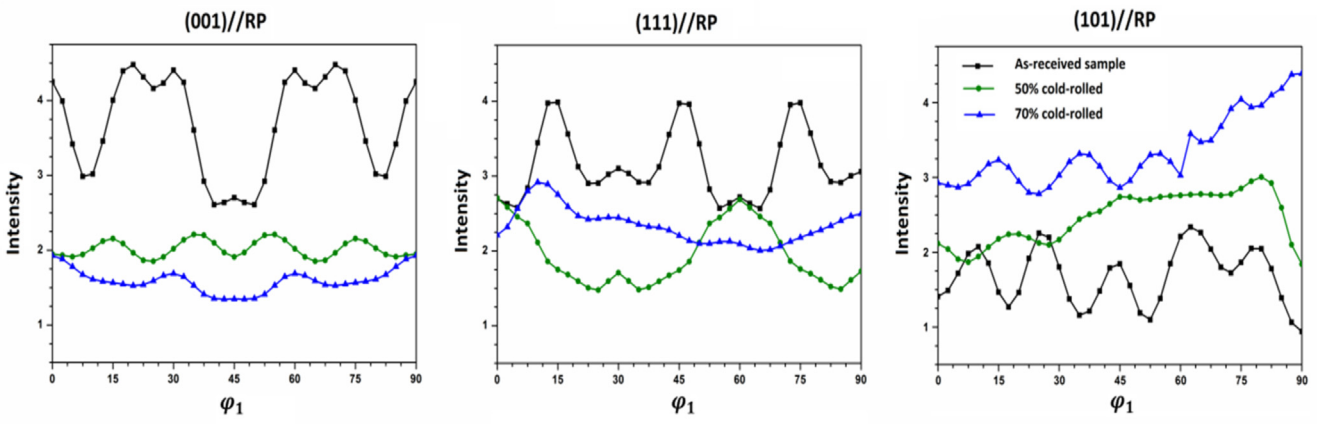

Fig. 4 – Skeleton plots of main fibres crystallographic texture (i.e (001)//RP (111)//RP, and (101)//RP) – RP: rolling plane of all investigated sample.

recrystallization during hot deformation [22]. Zhang et al. [23] reported that the {001}<120> components mainly originate during recrystallization of {001} columnar grains and exhibits a low mechanical and corrosion resistance. The results of the present investigation showed that (011)[0 $\bar{1}$ 1] and (221)[1 $\bar{1}$ 0] texture components were developed during cold-rolling to a 50% reduction. Rotated Goss (011)[0 $\bar{1}$ 1] texture component relate to α-fiber (<011>//RD) forms parallel to stress promoting the formation of slip bands during strain. The formation of deformation bands could be attributed to the activation of the different slip systems inside the grain. Thereby, it leads to the different sets of rotation associated with strain

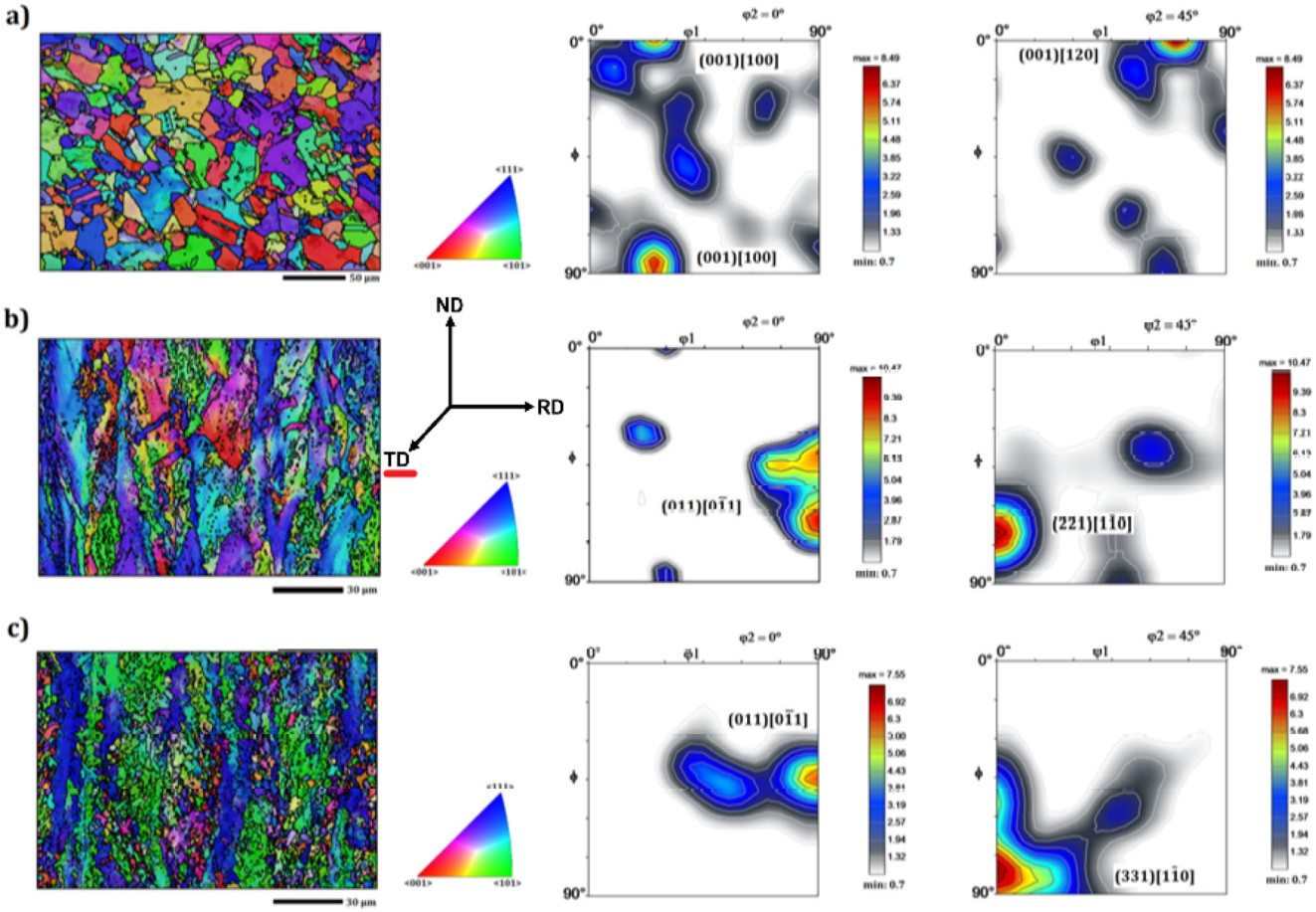

Fig. 5 – Orientation Image Maps and corresponding ODFs at constant $\varphi_2 = 0°$ and 45° sections of samples (a) as-received, cold-rolled to (b) 50% and (c) 70% reduction.

Table 1 – Grain boundaries characteristics in investigated specimens.

Type of grain boundaries	As-received	50% cold-rolled	70% cold-rolled
LABs ($2° < \Theta < 5°$)	0.31	0.43	0.49
MABs ($5° < \Theta < 15°$)	0.01	0.25	0.29
HABs ($15° < \Theta$)	0.68	0.32	0.22
CSLs	0.10	0.15	0.23

accommodation and crystallographic orientation [24]. Shamanian et al. [25] reported the presence of (221)[1 $\bar{1}$ 0] texture components in austenitic stainless steel by the reorientation of (001) grains toward loading direction under high strain due to the twinning deformation mechanism. With increasing the rolling reduction to 70%, (011)[0 $\bar{1}$ 1] and (331)[1 $\bar{1}$ 0] components were predominant. This can be attributed to the formation of subgrains and substructures in the austenite. Strong rotated Goss (011)[0 $\bar{1}$ 1] and (331)[1 $\bar{1}$ 0] components aligned <011>//RD fibre correlates well with the peak broadening in the (220)γ planes. No phase transformation occurred during cold rolling and it is notable a formation of sharp texture [25].

Point-to-point misorientation between two adjacent crystals represents the local plastic strain originated from the lattice distortion [26]. In contrast to transmission electron microscopy, the conventional EBSD technique is not able to visualize the spatial resolution below 100 nm. Thereby, the boundary misorientations of less than 2.0° cannot be reliable resolved [27]. Table 1 provides the fraction of low angle boundaries (LABs, $2° < \Theta < 5°$) medium angle boundaries (MABs, $5° < \Theta < 15°$), high angle boundaries (HABs, $15° < \Theta$), and coincidence site lattice (CSL) boundaries. The as-received hot rolled sample contains lowest fraction of low and medium angle misorientations due to dynamic recovery and recrystallization during the strip fabrication, allowing significant dislocation annihilation in this sample. The fraction of LABs and MABs is gradually increased by progressing degree of rolling reduction. High amount of dislocations and

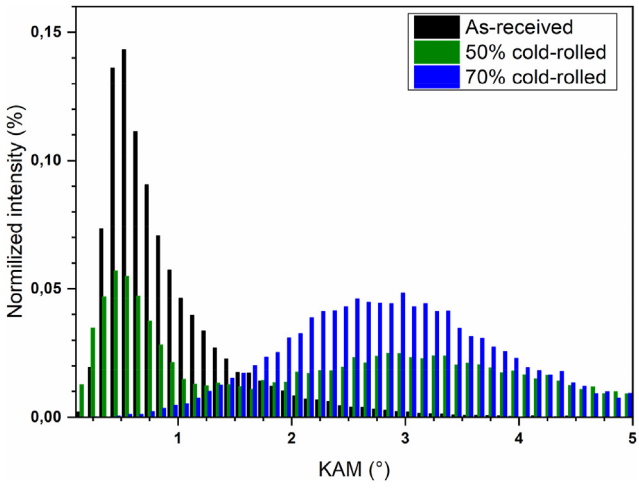

Fig. 6 – Kernel average misorientation distribution of all investigated specimens.

Table 2 – Variation of volume fractions of KAM values of investigated specimens.

KAM value	As-received	50% cold-rolled	70% cold-rolled
Low	0.70	0.34	0.01
Medium	0.29	0.33	0.55
High	0.01	0.33	0.44

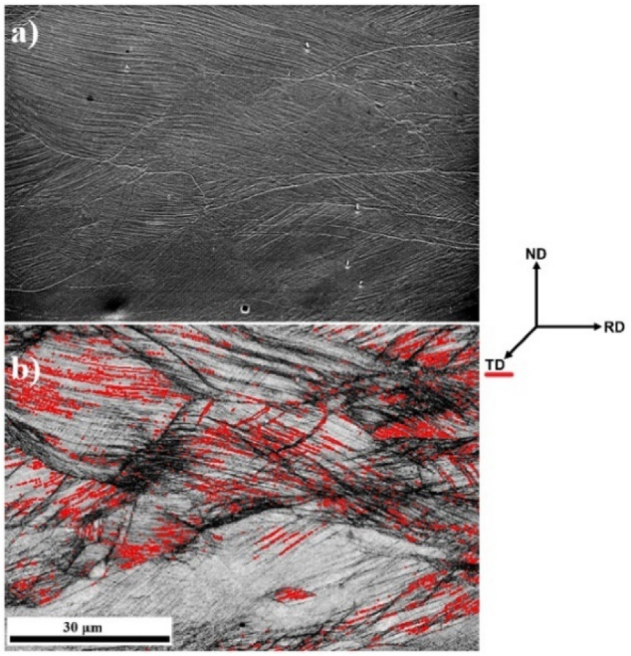

Fig. 7 – (a) SEM and (b) CLS boundaries map of 50% cold rolled sample.

Table 3 – Volumetric fraction of Σ CSL orientation relationships of investigated specimens.

Σ	Angle	Axis	Volumetric fraction (%)		
			as-received	50% cold rolled	70% cold rolled
3	60.0000	<111>	16.213	18.589	24.412
5	36.8699	<100>	0.172	0.211	0.298
7	38.2132	<111>	0.144	0.215	0.238
9	38.9424	<110>	1.653	0.653	0.943
11	50.4788	<110>	0.131	0.312	0.460
13a	22.6199	<100>	0.009	0.023	0.029
13b	27.7958	<111>	0	0.049	0.045
15	48.1897	<210>	0.115	0.098	0.208
17a	28.0725	<100>	0.034	0.025	0.020
17b	61.9275	<221>	0.087	0.193	0.250
19a	26.5254	<110>	0.034	0.041	0.051
19b	46.8264	<111>	0.062	0.066	0.087
21a	21.7868	<111>	0	0.006	0.012
21b	44.4153	<211>	0.065	0.210	0.193
23	40.4591	<311>	0.021	0.118	0.149
25a	16.2602	<100>	0.003	0.016	0.014
25b	51.6839	<331>	0.087	0.119	0.209
27a	31.5863	<110>	0.306	0.048	0.098
27b	35.4309	<210>	0.187	0.046	0.117
29a	43.6028	<100>	0.046	0.066	0.057
29b	46.3972	<221>	0.046	0.041	0.153
Sum			19.427	21.154	28.052

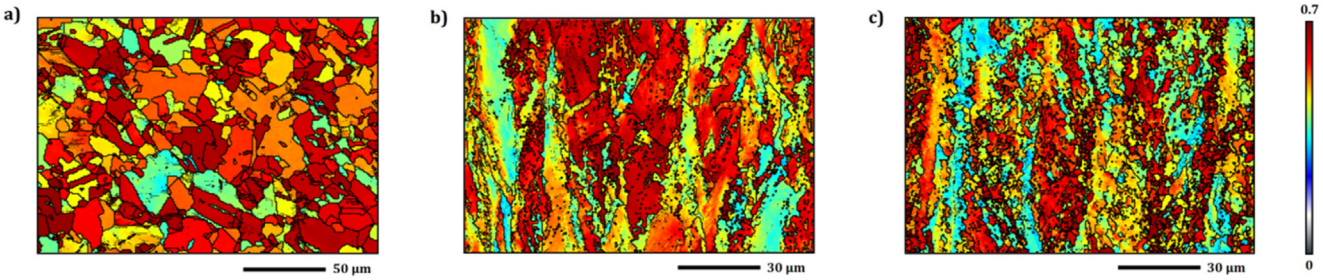

Fig. 8 – Schmid factor maps of samples (a) as-received, cold-rolled to (b) 50% and (c) 70% reduction.

crystallographic defects are generated during cold deformation-rolling. Dislocation cell boundaries are first formed, and then deformation-induced boundaries are developed by increased the amount of rolling reduction. Results showed that a gradual increase in misorientation inside the grain with progressing the rolling reduction led to grain fragmentation and re-oriented texture components. The development of low-energy CSL boundaries including $\sum 3^n$ twinning boundaries is commonly observed in austenitic steels [28]. The results of the present study also revealed that the highest portion of CSLs belongs to the 70% of cold rolled sample due to the formation of slip bands and deformation twins. Deformation-induced twinning in the cold-rolled samples could be associated with the planar slip bands as proposed by Guan et al. [29]. They suggested that planar-slip dislocation contains many Shockley partial dislocations that generate massive deformation twins by absorbing the planar-slip dislocations. Notably, the fraction of CSL boundaries increases with progressing the amount of deformation. The crystallographic anisotropy also plays a significant role in the development of lattice distortion including misorientation and this should be discussed on a grain-to-grain level. However, this is not the object of this study.

Although point-to-point misorientation refers to the relative orientation changes between two adjacent crystal orientations due to relative lattice rotation, the Kernel Average Misorientation (KAM) analysis evaluates misorientation between reference points with defined numbers of neighboring points within the grain. It is well known that the KAM analysis with a threshold of 5° has the purpose of eliminate the effect of subgrains [30]. Therefore, the strain distribution within the crystal grains can be estimated using the local change in orientation between third neighboring pixels following the KAM analyses. The quantitative results are shown in Fig. 6. The highest portion of low KAM values (KAM <1°) was found in the as-received sample. This could be attributed to the dynamic recrystallization with strain-free grains developed during hot deformation. With increased degree of cold-rolling reduction, a significant fraction of deformed grains with high medium (1° < KAM <3°) and high (KAM >3°) was developed. High values of KAM's could be associated with high local lattice distortion and dislocation density resulting in increasing of internal energy [31]. The as-received sample with recrystallized austenitic grains exhibited the lowest inter-granular misorientation within the microstructure. The formation of dislocation cells and dislocation tangles during cold-rolling increases the lattice distortion within the grain detected by KAM analyses. The local average misorientation distribution presented in Fig. 6 and Table 2 exhibits the variation of KAM values due to the misfit strains induced during deformation. Crystallographic defects such as dislocations, grain boundaries were responsible to developing the dislocation bands, low-angle boundaries and micro-twins. Thus, the localized stored strain energy due to lattice misfit acted as a barrier against dislocation glide which resulted in the increased strength accompanied by deterioration in ductility [31], that is discussed later in section 3.5.

Table 4 – Slip systems and their corresponding volume fractions.

Slip system	As-received	50% cold-rolled	70% cold-rolled
(1 1 $\bar{1}$) [0 1 1]	0.364	0.705	0.865
(1 1 $\bar{1}$) [1 0 1]	0.020	0.943	0.787
(1 1 $\bar{1}$) [1 $\bar{1}$ 0]	0.007	0.020	0.149
(1 $\bar{1}$ $\bar{1}$) [0 1 $\bar{1}$]	0.382	0.248	0.154
(1 $\bar{1}$ $\bar{1}$) [1 0 1]	23.145	13.828	19.034
(1 $\bar{1}$ $\bar{1}$) [1 1 0]	16.669	18.466	22.455
(1 $\bar{1}$ 1) [0 1 1]	16.003	16.261	16.416
(1 $\bar{1}$ 1) [1 0 $\bar{1}$]	0.544	0.346	0.250
(1 $\bar{1}$ 1) [1 1 0]	9.518	33.425	23.237
(1 1 1) [0 1 $\bar{1}$]	18.194	5.898	8.355
(1 1 1) [1 0 $\bar{1}$]	15.155	9.775	8.050
(1 1 1) [1 $\bar{1}$ 0]	0.002	0.084	0.250

3.4. *Electron back scattering diffraction (EBSD) analysis and coincidence site lattice (CSL) boundaries investigation*

The EBSD analysis was carried out to determine the volumetric fraction of CSL boundaries and quantify the increase in the probability of <111>formation and boundaries associated the mechanical twins. Although a gradual increase in the volume fraction of CSL boundaries was observed by increasing degree of the rolling reduction, more than 90% of CSL boundaries were attributed to the Σ3 deformation-induced twin boundaries. Fig. 7 shows the correlation with local slip bands formed under cold deformation with special boundaries identified by EBSD technique. Also, the volumetric fraction of low Σ CSL boundaries is listed in Table 3. In general, mechanical twins contribute to the superior mechanical properties of TWIP steels. Tokita et al. [32] reported enhanced mechanical properties by forming of the low-energy Σ3 twin boundaries during the thermomechanical processing which

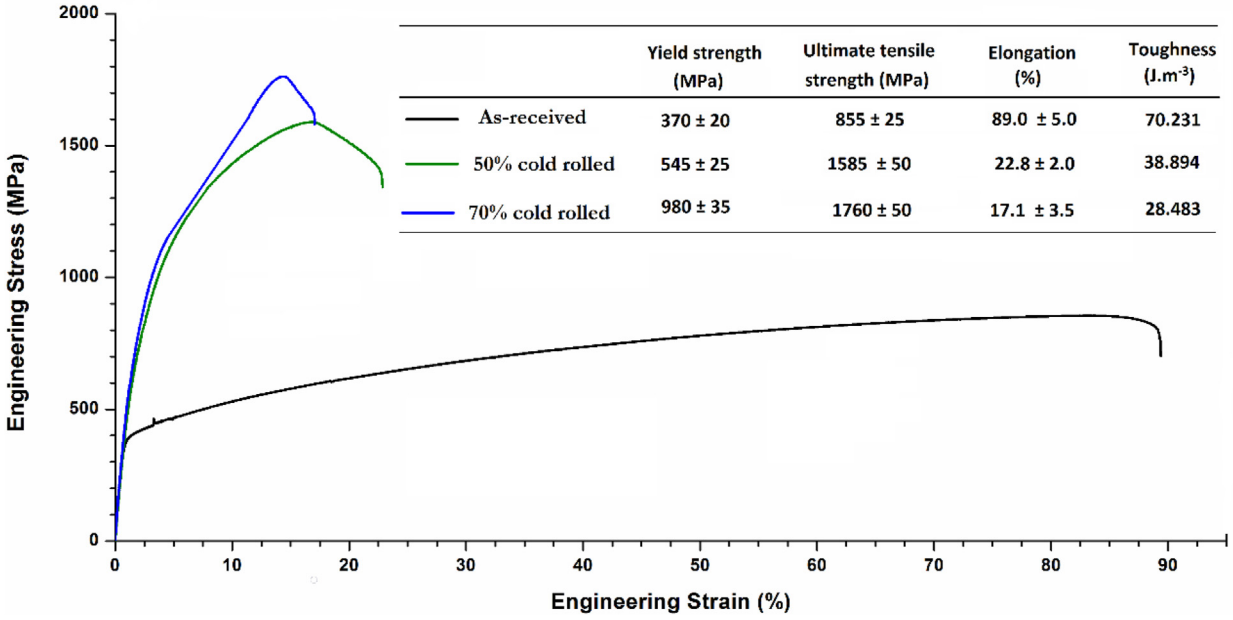

	Yield strength (MPa)	Ultimate tensile strength (MPa)	Elongation (%)	Toughness ($J.m^{-3}$)
As-received	370 ± 20	855 ± 25	89.0 ± 5.0	70.231
50% cold rolled	545 ± 25	1585 ± 50	22.8 ± 2.0	38.894
70% cold rolled	980 ± 35	1760 ± 50	17.1 ± 3.5	28.483

Fig. 9 – Engineering stress–strain curves.

reduces the total boundary energy in a triple junction. Shimada et al. [33] indicated that events and reactions of active twins increase the frequency of CSL boundaries. Well-distributed low-angle boundaries in the grain contour network create a discontinuous chain that can disrupt the percolation of intergranular surface corrosion, which is of interest to petroleum industry.

The activated slip systems of grains associated with the rolling direction were examined in terms of Schmid factor. The maximum value of Schmid factor during rolling was estimated to be 0.7, Fig. 8. The soft grains with high Schmid factor values tends to slip easily, while the hard grains (low Schmid factor) required higher shear stress to provide adequate slip systems required for deformation. Fig. 8 revealed that most of the grains in the 50% cold-rolled sample exhibited the Schmid factor values higher than 0.4, thereby, tend to deform easily. The fraction of grains with low Schmid factor values, see Fig. 8, increased after 70% cold rolling reduction. This is an indication that the material increased its resistance against plastic deformation under this last condition.

The FCC crystal structure contains 12 slip systems, considering four octahedral {111} planes with three close-packed <110> directions on each plane. The calculation of slip systems and their corresponding volume fractions in austenitic high-Mn steel according to the Lin and Ito [34] were carried out using the ATEX analysis software and results are listed in Table 4. Results showed that the same active slip systems, including (1 $\bar{1}$1)[101], (1 $\bar{1}$1)[110], (1 $\bar{1}$ 1)[011], (1 $\bar{1}$ 1)[110], (111)[01 $\bar{1}$], and (111)[10 $\bar{1}$], are common in all investigated specimens. According to the Von-Mises theory, at least five active slip systems are required for plastic deformation; thereby, the six mentioned activated slip systems prevent dislocation accumulation [35].

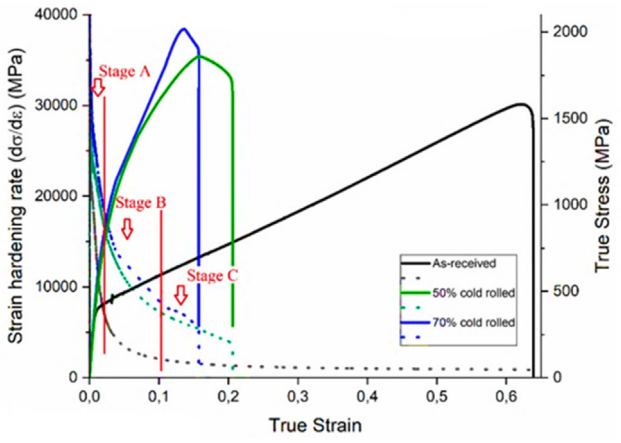

Fig. 10 – Strain hardening rate (dσ/dε)-true strain curve.

3.5. *Mechanical tensile tests*

Tensile tests were carried out to determine mechanical properties and these are presented in Fig. 9. Please note some serrated flows in tensile test curves of the as-received sample caused by the dynamic strain aging induced from interactions between partial dislocations and C–Mn clusters [36]. On the one hand, the yield stress, which was determined by the 0.2% offset method, and ultimate tensile strength significantly increased by increment in deformation degree. On the other hand, the total elongation drastically decreased from ~89% to 17% in the 70% cold-rolled sample. In the as-received sample the high elongation was associated with high glide planarity of dislocations in the austenitic matrix that enhances the TWIP effect during the tensile test. In addition, in the sample submitted to 70% cold-rolling a high level of lattice distortion was evidenced by XRD analysis, Fig. 2. This leads to both the highest tensile strength (1.7 GPa) and the highest strain hardening beside fine grain strengthening effect. Moreover,

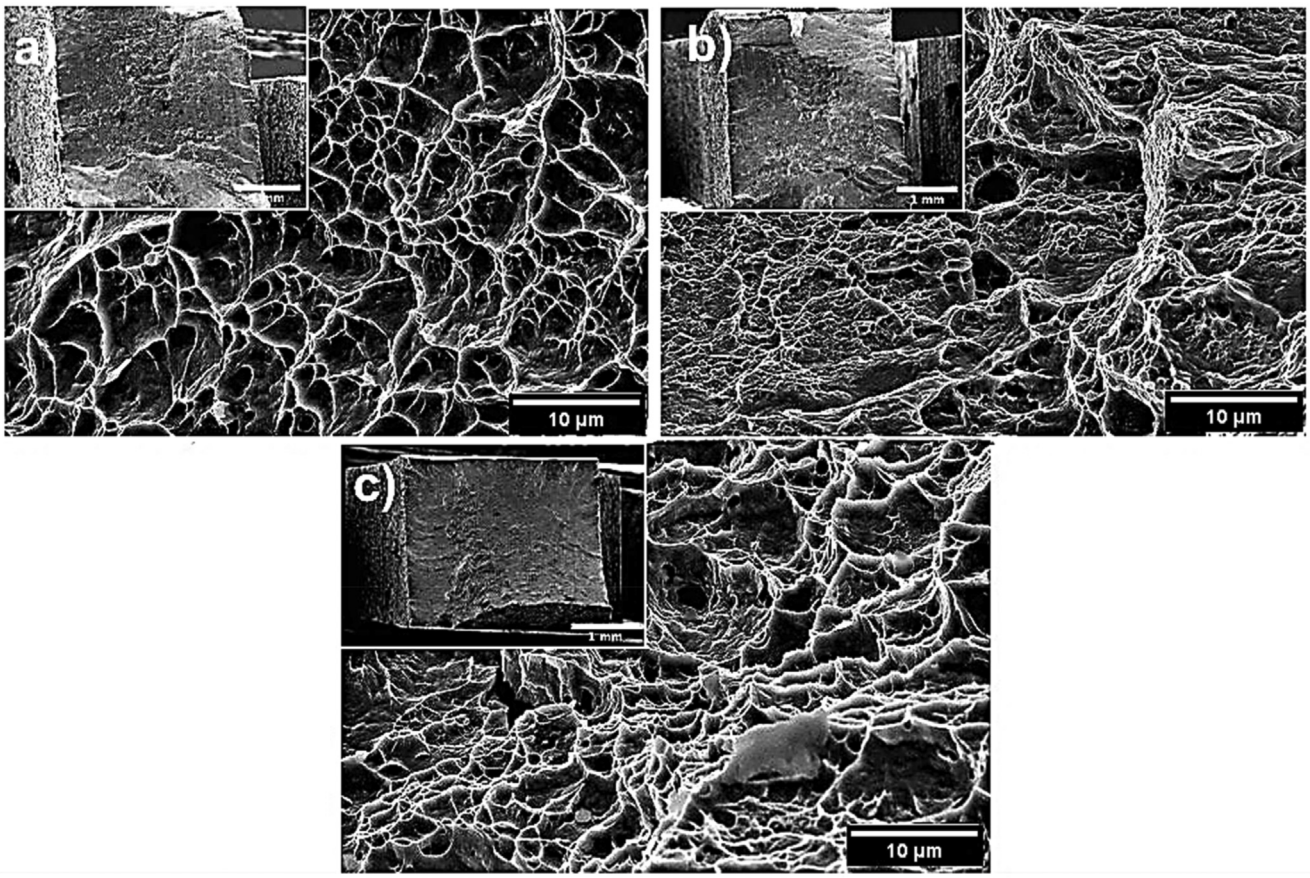

Fig. 11 – Fracture surfaces of the fractured tensile test specimens (a) as-received, (b) 50%, and (c) 70% cold-rolled.

the XRD and microstructure results revealed, that a fully austenitic structure remained in the 70% cold rolled samples despite the great quantity of deformation suffered by the material. The toughness, which were calculated from the area under the flow curves, decreased proportionally to the applied quantity of rolling deformation. The values remained high even with the refinement of the grain and highest tensile strength. It is noteworthy that the values reported by Skilbred et al. [37] regarding the yield stress, ultimate tensile strength and toughness for conventional Fe–C–Mn steels currently used in the petroleum industry are lower than those of cold-deformed samples of high-Mn steel investigated in this work. Thereby, a considerable mechanical and corrosion resistance (by the Cr and Cu contents) can be expected in these samples, for being purely austenitic, favoring application in petroleum industry [38–40].

Fig. 10 illustrates the true tensile stress, σ, and strain hardening rate curves ($d\sigma/d\varepsilon$) versus strain plots for the as-received specimen in addition to samples subjected to cold rolling. It is possible to verify that the samples tested obeyed the Considère criterion, which establishes that the maximum load is the point of the beginning of the formation of the "neck" in the test body (reduction of the cross-sectional area), where the strain hardening rate is equal to the tension. Specimens present strain hardening rate curves with three defined stages [41,42]. The plot of the as-received sample shows that the plastic deformation can be divided into three stages: first, a dramatic decrease in the strain range of 0–0.028 (Stage A) that corresponds to the elastic–plastic transition; second, a slight decrease until 0.12 strain (Stage B), which may be associated with plastic deformation governed by the slip of the dislocations, and finally, above 0.13 strain a decrease in hardening rate is observed by deformation (stage C). It interrupts the linear decline of the deformation hardening rate observed in stage B and delays the asymptotic approach for zero deformation hardening (constant state). This behavior is similar to the one found for TWIP steels, with no increase in the strain hardening rate during stage B and with its marginal decrease during stage C. The SFE values for the studied steel favored the mechanical twinning. This decrease is even more pronounced during secondary twinning since these systems are less active and this is reflected in lower strain hardening rates during stage B and especially in stage C when compared to other TWIP steels such as FeMnC TWIP steels [43–47].

The fracture surfaces samples were investigated, and are presented in Fig. 11. The fractography of as-received sample mainly contains the fibrous zone with some dimples with different sizes and depths and shear lip zone, indicating the good plastic deformation capacity. Dimple fracture mode corresponds to the nucleation and growth of micro-cracks originating at the intersection of slip bands and grain boundaries. Ren et al. [48] reported that the larger and deeper dimple improves the plastic deformation capacity. At the same time, some noticeable differences in fracture

morphology between the as-received and cold-rolled samples are observed. Although typical ductile fracture features were observed in the as-received sample, the brittle fracture facets were found in the cold-rolled specimens. Shear bands intersection shown in the deformed microstructure acts as favorable sites for micro-crack initiation due to the stress concentration. In addition, the induced misfit strains revealed by the Schmid factor analysis facilitate crack propagation by providing a low-energy transgranular crack trajectory, which is consistent with the low tensile ductility presented in Fig. 9. Notably, the ductile-brittle fracture mode observed in the 70% cold-rolled sample could be associated with formation of the high fraction of low-energy Σ3 twin boundaries, which minimized the localized stored strain energy and lattice misfit to promote dislocation glide.

4. Conclusions

This work focused on the evolution of the austenitic microstructure, crystallographic orientation, grain boundary features, and lattice distortions during cold rolling at room temperature of a Fe–26Mn-0.4C steel. The gradual development of the shear bands and a rise in dislocation density by increased degree of deformation promotes dislocation glide and twin-induced plasticity. Grain refinement coupled with increased fraction of low-energy Σ3 twin boundaries; i) increased local lattice distortion ii) reduced the cleavage (001) planes, thereby resulting in an acceptable balance between strength and elongation. Ultra-high strength austenitic TWIP steels can be considered as potential materials to be employed in the petroleum industry.

Declaration of Competing Interest

The authors declare that they have no known competing financial interests or personal relationships that could have appeared to influence the work reported in this paper.

Acknowledgement

The authors would like to thank Funcap (Cearense Foundation to Support Scientific and Technological Development) for the financial support for this research. This research used facilities of the Brazilian Nanotechnology National Laboratory (LNNano), part of the Brazilian Centre for Research in Energy and Materials (CNPEM), a private non-profit organization under the supervision of the Brazilian Ministry for Science, Technology, and Innovations (MCTI) under project SEM-C1-25167. Microstructural characterization of the specimens was performed at LNNano and the Central Analítica UFC/CT-INFRA-FINEP/Pro-Equipamentos-CAPES/CNPq-SisNano-MCTI 2019(Grant 442577/2019–2)-INCT-FUNCAP."-This study was financed in part by the Coordenação de Aperfeiçoamento de Pessoal de Nível Superior - Brasil (CAPES) - Finance Code 001."

REFERENCES

[1] V Malyar N, Kirchlechner C, Seok W, Sandl S, Korte-Kerzel S, Dehm G, et al. Dislocation interaction and twinning-induced plasticity in face- centered cubic Fe-Mn-C micro-pillars. Acta Mater 2017;132:162–73. https://doi.org/10.1016/j.actamat.2017.04.043.

[2] Zhi H, Zhang C, Antonov S, Yu H, Guo T, Su Y. Investigations of dislocation-type evolution and strain hardening during mechanical twinning in Fe-22Mn-0.6C twinning-induced plasticity steel. Acta Mater 2020;195:371–82. https://doi.org/10.1016/j.actamat.2020.05.062.

[3] Liu ZG, Gao XH, Xiong M, Li P, Misra RDK, Rao DY, et al. Role of hot rolling procedure and solution treatment process on microstructure, strength and cryogenic toughness of high manganese austenitic steel. Mater Sci Eng A 2021;807:140881. https://doi.org/10.1016/j.msea.2021.140881.

[4] Weon S, Hun J, Jik H, Min C, Soo C. Enhancing high-cycle fatigue properties of cold-drawn Fe-Mn-C TWIP steels. Int J Fatig 2016;85:57–64. https://doi.org/10.1016/j.ijfatigue.2015.12.007.

[5] lee Sangwon, Kim Jinkyung, Lee Seok-jae, De Cooman Bruno C. Effect of Cu addition on the mechanical behavior of austenitic twinning-induced plasticity. Steel Scripta Materialia 2011;65:1073–6. https://doi.org/10.1016/j.scriptamat.2011.09.019.

[6] Allain S, Chateau J-P, Bouaziz O, Migot S, Guelton N. Correlations between the calculated stacking fault energy and the plasticity mechanisms in Fe–Mn–C alloys. Mater Sci Eng, A 2004;387–389:158–62. https://doi.org/10.1016/j.msea.2004.01.059. ISSN 0921-5093.

[7] Dumay A, Chateau J-P, Allain S, Migot S, Bouaziz O. Influence of addition elements on the stacking-fault energy and mechanical properties of an austenitic Fe–Mn–C steel. Mater Sci Eng, A 2008;483–484:184–7. https://doi.org/10.1016/j.msea.2006.12.170. ISSN 0921-5093.

[8] Randall MG, Seong JP. Mathematical relations in ParticulateMaterials processing:ceramics, powder metals, cermets, Carbides,Hard materials, and minerals (Canada). Hoboken: Wiley; 2008.

[9] Chen J, Dong FT, Liu ZY, Wang GD. Grain size dependence of twinning behaviors and resultant cryogenic impact toughness in high manganese austenitic steel. J Mater Res Technol 2021;10:175–87. https://doi.org/10.1016/j.jmrt.2020.12.030.

[10] Florez MAC, S Lima MN, Araujo WS, Silva MJG. Mater Res-Ibero-AM J. 2019;22:2. https://doi.org/10.1590/1980-5373-MR-2019-0283.

[11] Kowalska J, Kowalski M. Development of microstructure and texture after cold-rolling Fe-24Mn-3Al-3Si high-manganese steel. J Mater Eng Perform 2020;29:1495–501. https://doi.org/10.1007/s11665-019-04516-y.

[12] Van Berkum JGM, Delhez R, de Keijser Th H, Mittemeijer EJ. Diffraction-line broadening due to strain fields in materials; fundamental aspects and methods of analysisx. Acta Crystallogr 1996;A52:730–47. https://doi.org/10.1107/S0108767396005727.

[13] Ye F, Zhu T, Mori K, Xu Q, Song Y, Wang Q, et al. Effects of dislocations and hydrogen concentration on hydrogen embrittlement of austenitic 316 stainless steels. J Alloys Compd 2021;876:160134. https://doi.org/10.1016/j.jallcom.2021.160134.

[14] Ungar T, Borbelt A. The effect of dislocation contrast on x-ray line broadening: a new approach to line profile Analysis. Appl Phys Lett 1996;69:3173. https://doi.org/10.1063/1.117951.

[15] Kestens LAI, Pirgazi H. Crystal structures Texture formation in metal alloys with cubic crystal structures. Mater Sci Technol 2016;32:1303–15. https://doi.org/10.1080/02670836.2016.1231746. ISSN.
[16] Masoumi M, Reis FEU, De Castro MO, Béres M, De Abreu HFG. Texture evolution and phase transformation of 25Cr-6Mo-5Ni experimental duplex stainless steel during hot and cold rolling. J Mater Res Technol 2017;6:232–40. https://doi.org/10.1016/j.jmrt.2017.01.001.
[17] De Cooman BC, Estrin Y, Kyu S. Twinning-induced plasticity (TWIP) steels. Acta Mater 2018;142:283–362. https://doi.org/10.1016/j.actamat.2017.06.046.
[18] Hirsch J, Lücke K. Mechanism of deformation and development of rolling textures in polycrystalline fcc metals-II. Simulation and interpretation of experiments on the basis of Taylor-type theories. Acta Metall 1988;36:2883–904. https://doi.org/10.1016/0001-6160(88)90173-3.
[19] de Moura AN, de Alcântara CM, de Oliveira TR, da Cunha MA, Machado MLP. Effect of cold rolling reduction on texture, recrystallization and mechanical properties of UNS S32304 Lean Duplex stainless steel. Mater Sci Eng A 2021;802:140577. https://doi.org/10.1016/j.msea.2020.140577.
[20] Bruna RG. Efeitos dos laminados a quente e a morno na microestrutura, textura e propriedades de aços baixo carbono. Rev Esc Minas 2011;64:57–62. https://doi.org/10.1590/S0370-44672011000100007.
[21] Kamali H, Xie H, Bi H, Chang E, Xu H, Yu H, et al. Deformation mechanism and texture evolution of a low-Ni Cr–Mn–N austenitic stainless steel under bending deformation. Mater Sci Eng A 2021;804:140724. https://doi.org/10.1016/j.msea.2020.140724.
[22] Zinovieva O, Zinoviev A, Romanova V, Balokhonov R. Three-dimensional analysis of grain structure and texture of additively manufactured 316L austenitic stainless steel. Addit Manuf 2020;36:101521. https://doi.org/10.1016/j.addma.2020.101521.
[23] Zhang N, Yang P, Mao W. {001}<120>-{113}<361> recrystallization textures induced by initial {001} grains and related microstructure evolution in heavily rolled electrical steel. Mater Char 2016;119:225–32. https://doi.org/10.1016/j.matchar.2016.08.009.
[24] Feng Z, Zecevic M, Knezevic M. Stress-assisted and strain-induced phase transformationkinetics laws implemented in a crystal plasticity model for predicting strain path sensitive deformation of austenitic steels. Int J Plast 2021;136:102807. https://doi.org/10.1016/j.ijplas.2020.102807.Received.
[25] Shamanian M, Eghlimi A, Eskandarian M, Szpunar JA. Interface microstructure across cladding of super duplex stainless steel with austenitic stainless steel buffer layer. Surf Coating Technol 2014;259:532–42. https://doi.org/10.1016/j.surfcoat.2014.10.034.
[26] Després A, Zecevic M, Lebensohn RA, Mithieux JD, Chassagne F, Sinclair CW. Contribution of intragranular misorientations to the cold rolling textures of ferritic stainless steels. Acta Mater 2020;182:184–96. https://doi.org/10.1016/j.actamat.2019.10.023.
[27] Schwartz AJ, Kumar M, Adams BL. Electron backscatter diffraction in materials science, 233. New York: Spring; 2000. https://doi.org/10.1007/978-1-4757-3205-4. Sprong.
[28] Beladi H, Rohrer GS. The distribution of grain boundary planes in interstitial free steel. Metall Mater Trans 2013;44:115–28. https://doi.org/10.1007/s11661-012-1393-0.
[29] Guan XJ, Shi F, Jia ZP, Li XW. Grain boundary engineering of AL6XN super-austenitic stainless steel: distinctive effects of planar-slip dislocations and deformation twins. Mater Char 2020;170:110689. https://doi.org/10.1016/j.matchar.2020.110689.
[30] Fujii T, Yamakawa R, Tohgo K, Shimamura Y. Materials Characterization Analysis of the early stage of stress corrosion cracking in austenitic stainless steel by EBSD and XRD. Mater Char 2021;172:110882. https://doi.org/10.1016/j.matchar.2021.110882.
[31] De Vincentis NS, Avalos MC, Benatti EA, Kliauga A, Brokmeier H, Bolmaro RE. Materials Characterization XRD and EBSD analysis of anisotropic microstructure development in cold rolled F138 stainless steel. Mater Char 2017;123:137–52. https://doi.org/10.1016/j.matchar.2016.11.018.
[32] Tokita S, Kokawa H, Sato YS, Fujii HT. In situ EBSD observation of grain boundary character distribution evolution during thermomechanical process used for grain boundary engineering of 304 austenitic stainless steel. Mater Char 2017;131:31–8. https://doi.org/10.1016/j.matchar.2017.06.032.
[33] Shimada M, Kokawa H, Wang ZJ, Sato YS, Karibe I. Optimization of grain boundary character distribution for intergranular corrosion resistant 304 stainless steel by twin-induced grain boundary engineering. Acta Mater 2002;50:2331–41. https://doi.org/10.1016/S1359-6454(02)00064-2.
[34] Lin TH, Ito M. Theoretical plastic distortion of a polycrystalline aggregate under combined and reversed stresses. J Mech Phys Solid 1965;13:103–15.
[35] Girard G, Frydrych K, Kowalczyk-gajewska K, Martiny M, Mercier S. Cyclic response of electrodeposited copper films . Experiments and elastic-viscoplastic mean-field modeling. Mech Mater 2021;153:103685. https://doi.org/10.1016/j.mechmat.2020.103685.
[36] Jo MC, Jo MC, Zargaran A, Sohn SS, Kim NJ, Lee S. Effects of Al addition on tensile properties of partially recrystallized austenitic TRIP/TWIP steels. Mater Sci Eng A 2021;806:140823. https://doi.org/10.1016/j.msea.2021.140823.
[37] Ellen Synnøve Skilbred, Signe Aarthun Lootz, Roy Johnsen. Hydrogen embrittlement susceptibility of steel armor wires for flexible pipes. Nace International. C2020-14489. https://onepetro.org/NACECORR/proceedings-abstract/CORR20/All-CORR20/NACE-2020-14489/445983.
[38] Cheng M, He P, Lei L, Tan X, Wang X, Sun Y, et al. Comparative studies on microstructure evolution and corrosion resistance of 304 and a newly developed high Mn and N austenitic stainless steel welded joints. Corrosion Sci 2021;183:109338. https://doi.org/10.1016/j.corsci.2021.109338.
[39] Wang H, Yu H, Kondo S, Okubo N, Kasada R. Corrosion behaviour of Al-added high Mn austenitic steels in molten lead bismuth eutectic with saturated and low oxygen concentrations at 450 °C. Corrosion Sci 2020;175:108864. https://doi.org/10.1016/j.corsci.2020.108864.
[40] Li X, Liu J, Xiong J, Yang L, Gou Q, Song X, et al. Wear and corrosion resistant Mn-doped austenitic cast iron prepared by powder metallurgy method. J Mater Res Technol 2020;9:6376–85. https://doi.org/10.1016/j.jmrt.2020.03.099.
[41] Renard K, Jacques PJ. On the relationship between work hardening and twinning rate in TWIP steels. Mater Sci Eng A 2012;542(8– 14). https://doi.org/10.1016/j.msea.2012.01.123.
[42] Kusakin PS, Kaibyshev RO. High-Mn twinning-induced plasticity steels:Microstructure and mechanical properties. Rev Adv Mater Sci 2016;44(4):326–60. ISSN: 16065131.
[43] Barbier D, Gey N, Allain S, Bozzolo N, Humbert M. Analysis of the tensile behavior of a TWIP steel based on thetexture and microstructure evolutions. Mater Sci Eng A 2009:196–206. https://doi.org/10.1016/j.msea.2008.09.031.
[44] Jin Je, Lee YK. Strain hardening behavior of a Fe–18Mn–0.6C–1.5Al TWIP steel. Mater Sci Eng A

2009;A527:157–61. https://doi.org/10.1016/j.msea.2009.08.028.

[45] Jin Je, Lee YK. Effects of Al on microstructure andtensile properties of C-bearing highMn TWIP steel. Acta Mater 2012;60:1680–8. https://doi.org/10.1016/j.actamat.2011.12.004.

[46] Gutierrez-Urrutia I, Raabe D. Dislocation and twinsubstructure evolution during strainhardening of an Fe–22 wt% Mn–0.6 wt % C TWIP steel observed by electronchanneling contrast imaging. Acta Mater 2011;59:6449–62. https://doi.org/10.1016/j.actamat.2011.07.009.

[47] Jang Min Ji, Ahn Dong-Hyun, Moon Jongun, Bae Jae Wung, Yim Dami, Yeh Jien-Wei, et al. Constitutive modeling of deformation behavior of high-entropy alloys with face-centered cubic crystal structure. Mater Res Lett 2017;5(5):350–6. https://doi.org/10.1080/21663831.2017.1292325.

[48] kuan Ren J, yuan Chen Q, Chen J, yu Liu Z. Role of vanadium additions on tensile and cryogenic-temperature charpy impact properties in hot-rolled high-Mn austenitic steels. Mater Sci Eng A 2021;811:141063. https://doi.org/10.1016/j.msea.2021.141063.